# Low-Loss Integrated Nanophotonic Circuits with Layered Semiconductor Materials

Jijun He,[∥] Ioannis Paradisanos,[∥] Tianyi Liu, Alisson R. Cadore, Junqiu Liu, Mikhail Churaev, Rui Ning Wang, Arslan S. Raja, Clément Javerzac-Galy, Philippe Roelli, Domenico De Fazio, Barbara L. T. Rosa, Sefaattin Tongay, Giancarlo Soavi, Andrea C. Ferrari,* and Tobias J. Kippenberg*
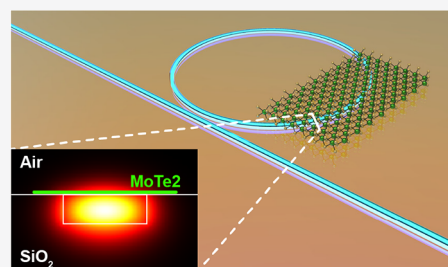
Cite This: *Nano Lett.* 2021, 21, 2709–2718

Read Online

ACCESS | Metrics & More | Article Recommendations

**ABSTRACT:** Monolayer transition-metal dichalcogenides with direct bandgaps are emerging candidates for optoelectronic devices, such as photodetectors, light-emitting diodes, and electro-optic modulators. Here we report a low-loss integrated platform incorporating molybdenum ditelluride monolayers with silicon nitride photonic microresonators. We achieve microresonator quality factors $>3 \times 10^6$ in the telecommunication O- to E-bands. This paves the way for low-loss, hybrid photonic integrated circuits with layered semiconductors, not requiring heterogeneous wafer bonding.

Layered materials (LMs),[1] such as graphene, transition-metal dichalcogenides (TMDs), and black phosphorus, are emerging platforms for applications in microelectronics,[2−4] nanophotonics,[5−8] and optoelectronics.[9−12] Particularly important for optoelectronics are LMs with direct bandgaps, such as monolayer (1L) TMDs, enabling new physics and applications such as valleytronics,[13] spintronics,[14] transistors,[15] light-emitting diodes (LEDs),[16] modulators,[10] and photodetectors.[11] Semiconducting TMDs undergo an indirect-to-direct bandgap transition when exfoliated from bulk to 1L,[17,18] and their optical properties are dominated by excitonic transitions,[19−21] typically in the visible or near-infrared ranges. E.g., 1L molybdenum diselenide (1L-MoSe₂) has a bandgap ∼1.7 eV[22] (∼730 nm), and for 1L molybdenum ditelluride (1L-MoTe₂) this is ∼1.1 eV[23,24] (∼1130 nm).

Strong light−matter interaction with LMs is beneficial for optoelectronics applications. One approach to enhance it is to integrate LMs with low-loss photonic microresonators.[25−29] E.g., photodetectors employ resonant structures to significantly enhance the photon absorption and responsivity.[30] The performance of a microresonator depends not only on the mode volume, but also on the quality factor, defined as $Q = \omega/\kappa$, where $\omega/2\pi$ is the frequency of the optical mode and $\kappa/2\pi$ is the resonance line width.[31] $Q$ is a dimensionless parameter describing the energy stored in the microresonator divided by the energy dissipation per round trip.[31] Thus, $Q$ represents the power storing capability of a microresonator (i.e., the intracavity power enhancement with respect to the external optical field). In addition, $Q$ is related to the intrinsic quality factor $Q_0$ (determined by light absorption and

scattering within the microresonator[32]) and the external coupling $Q_{ex}$ (determined by how strong the microresonator is coupled to the external optical field[33]), as $Q^{-1} = Q_0^{-1} + Q_{ex}^{-1}$.
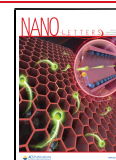
Planar photonic integrated circuits (PICs) are ideal platforms to enhance light−matter interactions with 1L-TMDs and to build new classes of high-performance integrated devices, such as LEDs, modulators, and photodetectors. The planarized top surfaces of waveguides and microresonators are advantageous, as the 1L-TMDs' flatness is maintained and strain-induced local fluctuations in the 1L-TMDs' band structure[34] are avoided. With deterministic transfer of 1L-TMDs,[35] these devices could be fabricated using CMOS technology with high yields[7] and large volumes.[36] For most 1L-TMDs, their bandgaps for excitonic transitions lie in the visible range, while silicon (Si), commonly used in integrated photonics, has a transparency window[37] > 1.2 μm. This makes Si-based devices challenging for applications using TMDs, such as visible LEDs.

Silicon nitride (Si₃N₄)[38,39] is a promising alternative to Si. It has a bandgap ∼5 eV,[40] enabling a transparency window covering 400−2500 nm, free from two-photon absorption in the telecommunication bands. Refs. 41−45 reported inte-
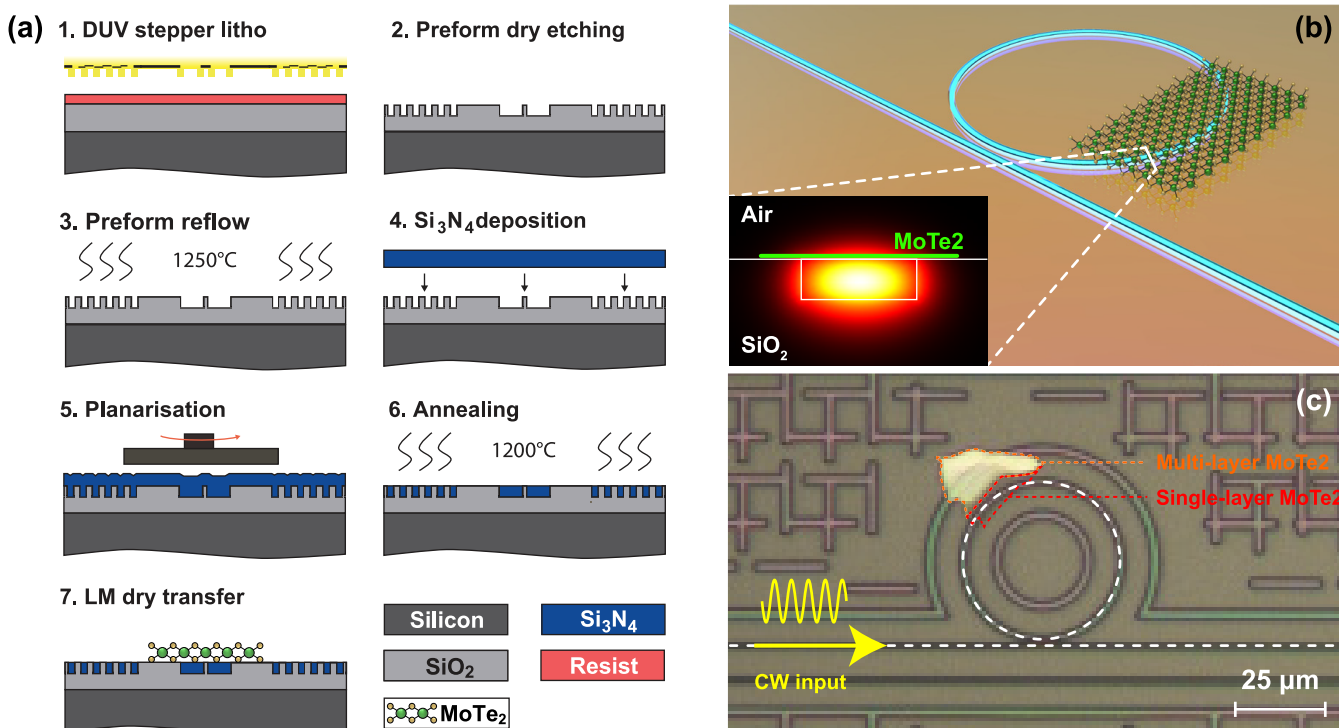
**Figure 1.** Fabrication process flow and sample overview. (a) Photonic Damascene reflow process to fabricate air-cladded, high-$Q$, $Si_3N_4$ microresonators and integration of 1L-$MoTe_2$. 1. Deep-UV stepper lithography is used to pattern the $Si_3N_4$ structures. 2. The pattern is transferred from the photoresist mask to the $SiO_2$ substrate via dry etching. 3. A preform reflow at 1250 °C reduces the waveguide sidewall roughness. 4. LPCVD $Si_3N_4$ is deposited on the patterned substrate, filling the trenches and forming the $Si_3N_4$ structures. 5. The excess $Si_3N_4$ is removed by CMP, ensuring a flat top surface. 6. The substrate is annealed at 1200 °C to drive out the residual hydrogen content in $Si_3N_4$. 7. Dry transfer of LMs onto the $Si_3N_4$ microresonator. (b) Schematic of $Si_3N_4$ microring resonator covered with 1L-$MoTe_2$. (c) Optical microscope image showing $Si_3N_4$ microring resonator, bus waveguide, and $MoTe_2$. The white dashed line marks the $Si_3N_4$ ring resonator and bus waveguide, where light propagates.

grated $Si_3N_4$ waveguides with tight optical confinement and low losses ~1 dB/m, enabling microresonators with $Q$[42,45] >30 × $10^6$ and 1 m-long spiral waveguides in 20 $mm^2$ footprints.[45] In comparison, the lowest optical losses are still >35 dB/m for both Si[46] and indium phosphide (InP)[47] because of the fabrication processes and the high refractive indices ($n_{Si}$ = 3.5 and $n_{InP}$ = 3.2 measured at the telecommunication bands) that enhance light scattering at the waveguide surface. $Si_3N_4$ has an excellent handling capability for high optical power >100 kW.[48] Combining the high nonlinear index $n_2$ = 2.5 × $10^{-15}$ $cm^2W^{-1}$ (describing the refractive index change induced by the optical intensity)[38] and the established geometry dispersion engineering (i.e., tailoring the group-velocity dispersion via geometry variation[49]), $Si_3N_4$ has been used for various linear and nonlinear photonics applications based on light-matter interactions, particularly for microresonator-based Kerr frequency combs[50] and chip-based supercontinuum generation.[51] Low-loss $Si_3N_4$ PICs are promising to study light−matter interactions with TMDs[52,53] and have already been used to build modulators[29] and photodetectors.[54,55] These active devices are also important for $Si_3N_4$ photonics, as $Si_3N_4$ is insulating and passive.

Here, we integrate $Si_3N_4$ microresonators with 1L-$MoTe_2$ and investigate the optical response of this $Si_3N_4$-TMD hybrid system. 1L-$MoTe_2$ has an bandgap ~1.1 eV (~1130 nm[23,24]). Thus, it is essentially transparent in the telecommunication bands 1280 - 1630 nm. We use photonic chip-based $Si_3N_4$ microring resonators with free spectral ranges (FSR, i.e. frequency spacing of the optical resonance grid) of 150 GHz

and 1 THz. The FSR = $D_1/2\pi$, is calculated from the resonant condition $D_1/2\pi = c/(2\pi R \cdot n_g)$,[56] where $c$ is the speed of light in vacuum and $n_g$ is the group index of the optical mode ($c/n_g$ being the group velocity of light). The $Si_3N_4$ microresonators, fabricated using the photonic Damascene process,[57] have no top $SiO_2$ cladding, thus the 1L-$MoTe_2$ transferred onto the $Si_3N_4$ waveguide's top surface can directly interact with the optical mode in the waveguide core.

Figure 1a presents the fabrication process flow for our $Si_3N_4$ PICs with LMs. The $Si_3N_4$ PIC is fabricated using the photonic Damascene process.[57] Deep-UV stepper lithography based on KrF at 248 nm is used to pattern $Si_3N_4$ waveguides, microresonators, and stress-release structures[57] (to prevent crack formation in $Si_3N_4$ due to the tensile film stress). The pattern is transferred from the photoresist mask to the $SiO_2$ substrate using dry etching based on $C_4F_8$, $O_2$, and He, followed by a preform reflow[58] at 1250 °C to reduce the waveguide surface roughness. Low-pressure chemical vapor deposition (LPCVD) based on $SiH_2Cl_2$ and $NH_3$ is used to deposit stoichiometric $Si_3N_4$ on the patterned preform, filling the trenches and forming the waveguide cores. The excess $Si_3N_4$ is removed by chemical-mechanical polishing (CMP), creating a flat top surface with a root-mean-square (RMS) roughness <0.3 nm,[58] ideal to maintain the 1L-TMDs' flatness. The substrate is then annealed at 1200 °C to drive out the residual hydrogen introduced during LPCVD. There is a height difference <40 nm between the $Si_3N_4$ waveguide cores and the surrounding $SiO_2$ cladding, as measured by scanning electron microscopy (SEM) and atomic force
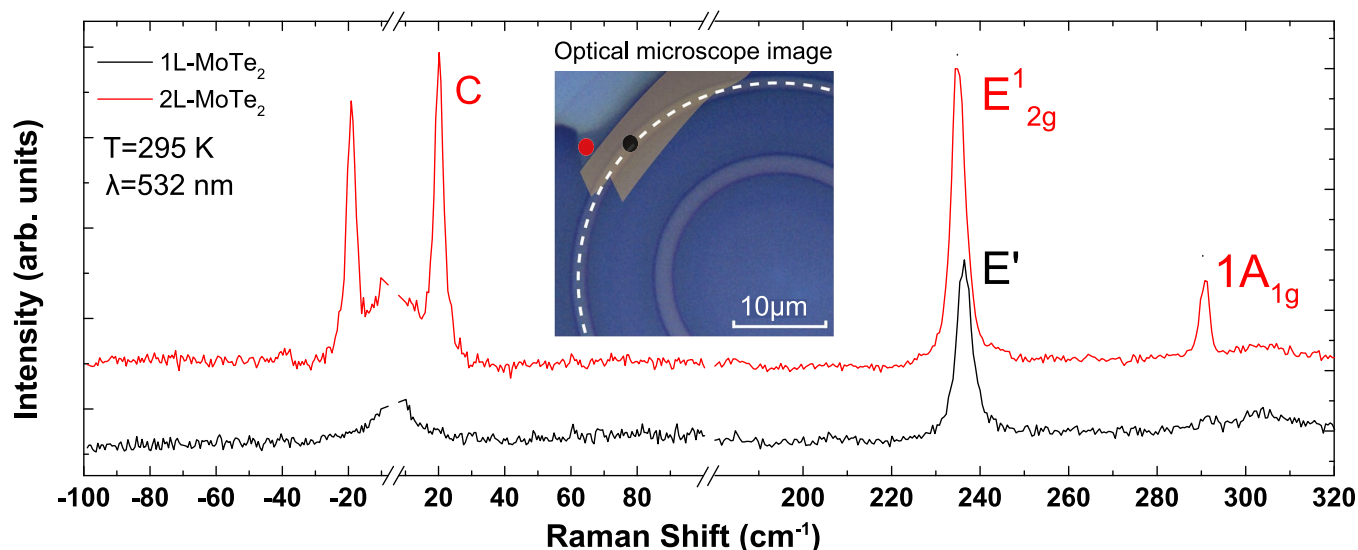
**Figure 2.** Raman spectra of 1L-MoTe$_2$(black) on microresonator and 2L-MoTe$_2$(red) outside it. Inset: optical microscope image of 1L-MoTe$_2$ on a Si$_3$N$_4$ microresonator. The black and red spots indicate where the representative Raman spectra of 1L- and 2L-MoTe$_2$ were measured. The white dashed line marks the Si$_3$N$_4$ microresonator, and the gray area is the 1L-MoTe$_2$ flake.

microscopy (AFM). This is caused by the post-CMP cleaning using buffered HF to remove the CMP slurry particles, and can be reduced by optimizing the cleaning process. The Si$_3$N$_4$ waveguides without top SiO$_2$ cladding allow seamless contact of 1L-MoTe$_2$ with the optical mode via evanescent coupling. This feature is a key advantage of the photonic Damascene process because of its additive fabrication nature. In comparison, the top-down, subtractive process[59,60] requires complex control of the planarization, in order to create a flat wafer surface with bare waveguides.

1L-MoTe$_2$ flakes are exfoliated from bulk 2H-MoTe$_2$ crystals (alpha phase) prepared by flux zone growth[61] on Nitto Denko tape[17] and then exfoliated again on a polydimethylsiloxane (PDMS) stamp placed on a glass slide for inspection under an optical microscope. Optical contrast is used to identify 1L-MoTe$_2$ prior to transfer.[62] Before 1L-MoTe$_2$ transfer, the Si$_3$N$_4$ microresonators are wet-cleaned by 60 s ultrasonication in acetone and isopropanol and exposed to oxygen-assisted plasma at 10 W for 60 s. The 1L-MoTe$_2$ flakes are aligned and stamped on the Si$_3$N$_4$ microresonators with a micromanipulator at 40 °C, before increasing the temperature to 60 °C, so the flakes detach from the PDMS and adhere preferentially to the microresonators.[63] Figure 1b illustrates a Si$_3$N$_4$ microring resonator covered with 1L-MoTe$_2$. Figure 1c shows the optical microscope image of the sample, with the white dashed line marking the Si$_3$N$_4$ bus waveguide and the microring resonator. Light is coupled from the bus waveguide to the microring resonator via in-plane evanescent coupling with a gap distance of 775 nm.

To characterize the transferred 1L-MoTe$_2$, we use micro-Raman spectroscopy at 532 nm (~2.3 eV), close to the C-exciton energy of MoTe$_2$,[64] to enhance the electron−phonon interaction[65,66] in the vicinity of the Γ-point of the Brillouin zone. We use <50 μW power to avoid thermal effects. The measurements are performed in a Horiba LabRam Evolution with a cutoff frequency ~5 cm$^{-1}$, a 1800 l/mm grating and a spot size ~700 nm. We measure 1L-MoTe$_2$ located on the microresonator (black dot in the inset of Figure 2), and compare it with a 2L-MoTe$_2$ flake out of the microresonator (red dot in the inset of Figure 2). The Raman spectra of 1L-

and 2L-MoTe$_2$ are also shown in Figure 2. A strong C mode[67,68] is observed ∼ 19.5 cm$^{-1}$ in 2L-MoTe$_2$ but is absent for 1L-MoTe$_2$, as expected.[69] The in-plane modes are ∼ 236.4 cm$^{-1}$ for 1L-MoTe$_2$ (E' mode) and ∼234.9 cm$^{-1}$ for 2L-MoTe$_2$ (E$_{2g}^1$ mode), in good agreement with literature.[70] The out-of-plane metal-chalcogen vibration (B$_{2g}$ in bulk and 1A$_{1g}$ in 2L-MoTe$_2$[70]) is only observed in 2L-MoTe$_2$ ∼290.8 cm$^{-1}$, because B$_{2g}$ symmetry modes are inactive for 1L-MoTe$_2$.[70] This confirms the transfer of 1L-MoTe$_2$ on the microresonator.

To investigate the effect of the transferred 1L-MoTe$_2$ on the Si$_3$N$_4$ optical mode, we characterize the optical resonances of the integrated hybrid microresonator system. For integrated photonics, a comprehensive characterization of the optical properties of any passive devices often includes the real and imaginary parts of the effective refractive index, $n_{eff}$ and $k_{eff}$ (thus the full effective refractive index is $n_{eff} + ik_{eff}$).[29] For microresonators, $n_{eff}$ and $k_{eff}$ can be obtained from measuring the frequencies $\omega/2\pi$ and line widths $\kappa_0/2\pi$ of the resonance grid.[32] These parameters are related via $Q_0 = \omega/\kappa_0 = n_{eff}/(2k_{eff})$. While the excitonic absorption of 1L-MoTe$_2$ in the telecommunication bands should be negligible, an increase of $k_{eff}$ is expected as a result of transfer-induced extra optical loss. This is due to the imperfect transfer of 1L-MoTe$_2$ that can cause contamination or surface damage. Thus, the change of $k_{eff}$ (i.e., $\Delta k_{eff}$) can be determined by measuring the line width increase or $Q$ factor decrease before and after TMD transfer. Figure 3a shows our optical characterization setup. Light is coupled into and out of the Si$_3$N$_4$ chip using lensed fibers and double-inverse nanotapers at the chip facets.[71] The total fiber-chip-fiber through coupling efficiency, i.e. the ratio of the optical power in the output fiber to the power in the input fiber, is ~40%. To measure $\omega/2\pi$ and $\kappa_0/2\pi$, the optical transmission spectrum of the microresonator is calibrated using frequency-comb-assisted diode laser spectroscopy.[72,73] Three mode-hop-free, widely tunable, external-cavity diode lasers (ECDLs) are used and cascaded[73] to cover the telecommunication O- to E-band (1280−1630 nm). When scanning, the instantaneous laser frequency is acquired by beating the laser with a commercial, self-referenced, fiber-
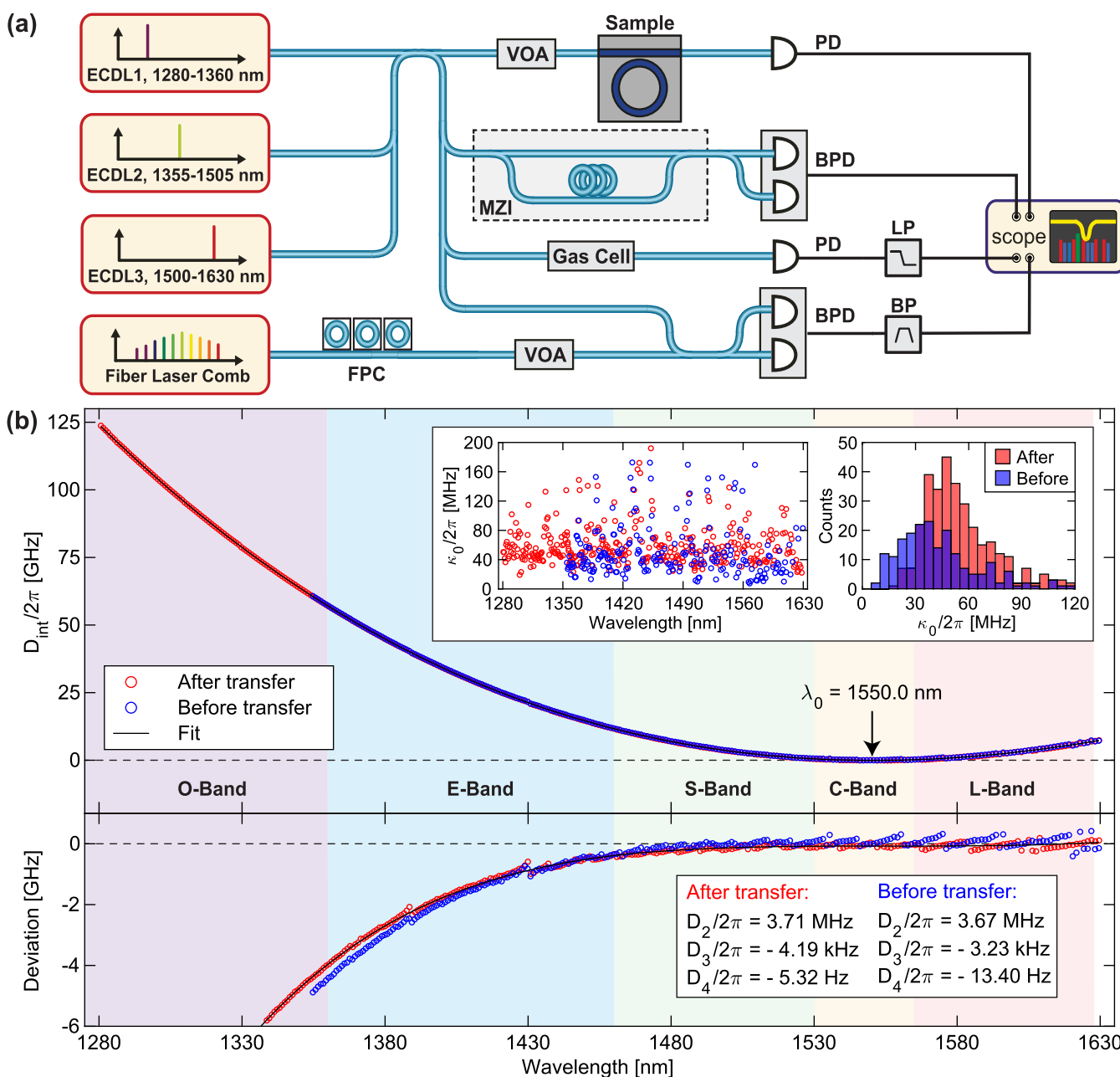
**Figure 3.** Experimental characterization of loss and dispersion of 150-GHz-FSR $Si_3N_4$ microresonator. (a) Frequency-comb-assisted cascaded diode laser spectroscopy used to characterize the microresonator. ECDL: external-cavity diode laser. FPC: fiber polarization controller. VOA: variable optical attenuator. MZI: Mach−Zehnder interferometer. PD(BPD): (balanced) photodetector. LP/BP: electronic low/band-pass filter. (b) Top: Measured integrated microresonator dispersion profile, $D_{int}/2\pi$, covering 1280 - 1630 nm for the $TE_{00}$ mode. The reference resonance wavelength is 1550 nm. Insets: $\kappa_0/2\pi$ of each resonance, and $\kappa_0/2\pi$ histograms showing that the most probable value increases from 35 to 50 MHz after 1L-$MoTe_2$ transfer. Bottom: Resonance frequency deviation from the $D_2$-dominant parabolic profile $[D_{int}(\mu) - D_2\mu^2/2]/2\pi$, to reveal the change in higher-order dispersion (such as $D_3/2\pi$) and avoided mode crossings.

laser-based optical frequency comb,[72] assisted with a Mach−Zehnder interferometer.[57] Molecular absorption spectroscopy is also performed during the laser frequency scan,[73] to further calibrate the optical transmission spectrum of the microresonator, in order to extract the absolute frequency of each data point.

The light polarization is constant during the laser scan, as polarization-maintaining fiber components are used. Optical resonances in the microresonator transmission spectrum are identified and fitted,[74] to extract the microresonator's intrinsic loss $\kappa_0/2\pi$ and the bus-waveguide-to-microresonator external

coupling strength $\kappa_{ex}/2\pi$. The loaded line width is thus calculated as $\kappa/2\pi = \kappa_{ex}/2\pi + \kappa_0/2\pi$ ($\kappa$, $\kappa_{ex}$, and $\kappa_0$ are angular frequencies). Compared with previous studies on TMD-enabled PICs which analyzed the optical loss on a single wavelength[59] or a single resonance,[60] our optical characterization technique provides broadband wavelength-dependent information on $n_{eff}(\lambda)$ and $k_{eff}(\lambda)$, and can identify any absorption feature within the measurement band. Our transfer technique can thus be systematically optimized to achieve the lowest transfer-induced optical losses.
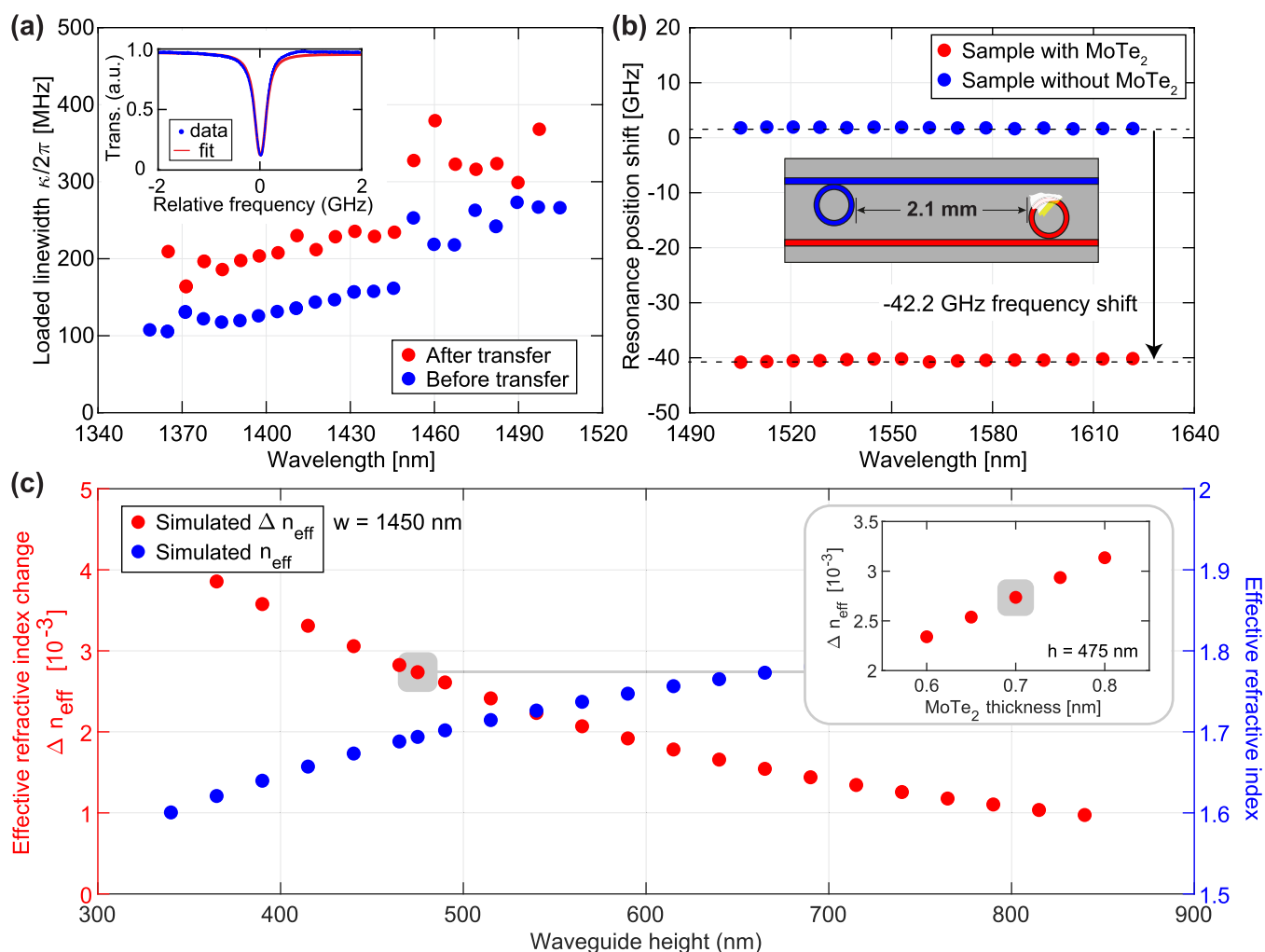
**Figure 4.** Experimental characterization and simulations of loss and resonance frequency shift of 1-THz-FSR $Si_3N_4$ microresonator with 1L-$MoTe_2$. (a) Measured $\kappa/2\pi$ before and after 1L-$MoTe_2$ transfer. Inset: representative resonance profile at 1425 nm and its Lorentzian fit, giving $\kappa_{ex}/2\pi$ = 82 MHz and $\kappa_0/2\pi$ = 147 MHz. (b) Measured and calculated absolute frequency shift of the $TE_{00}$ resonance grid before and after 1L-$MoTe_2$ transfer, for two microresonators, one with 1L-$MoTe_2$ and the other without. Inset: schematic showing that the two microresonators are 2.1 mm apart on the same chip. (c) Simulated $n_{eff}$ and change $\Delta n_{eff}$ of $n_{eff}$ due to the presence of 1L-$MoTe_2$, as a function of $Si_3N_4$ waveguide height. The simulated wavelength is 1550 nm in the $TE_{00}$ mode in the 1-THz-FSR microresonator. Insets: simulated $\Delta n_{eff}$ as a function of the $MoTe_2$ thickness.

1L-$MoTe_2$ flakes are transferred onto $Si_3N_4$ microresonators with two FSRs: 150 GHz and 1 THz. First, we characterize the 150-GHz-FSR microresonator. Here we mainly study the transverse-electric fundamental mode of the microresonator ($TE_{00}$ mode). We note that the transverse-magnetic fundamental mode ($TM_{00}$) has a higher loss than the $TE_{00}$ mode. We characterize the same $Si_3N_4$ microresonator before and after 1L-$MoTe_2$ transfer, for comparison and to extract any extra loss introduced by 1L-$MoTe_2$ transfer. The measured $\kappa_0/2\pi$ are plotted in the inset of Figure 3b. No wavelength-dependent $\kappa_0/2\pi$, before and after the transfer, is observed far above the 1L-$MoTe_2$'s excitonic resonance ~1130 nm.[23] Histograms of $\kappa_0/2\pi$ show that the most probable value increases from 35 to 50 MHz after transfer. This loss increment corresponds to a $Q_0$ degradation from 5.5 × $10^6$ to 3.9 × $10^6$, representing a viable low-loss microresonator with TMD integration. To the best of our knowledge, this is the highest $Q$ reported in LM-enabled PICs. Ref 75 pointed out that the transfer process can affect the transmission properties of a photonic device to such an extent that no transmission can be measured. E.g. mechanical scratches or contaminations on the chip surface can be the loss sources.[76] Since our microresonator $Q$ is high (~5.5 × $10^6$, corresponding to 6 dB/m linear loss) and our loss characterization method is accurate, any loss increment down to the level of dB/m can be observed. This enables us to improve our LM transfer to minimize losses. The LM surface cleanness is mostly associated with the speed and temperature used for transfer.[77,78] With PDMS transfer, we were able to detect interlayer excitons in TMD-LM heterostructures (LMHs),[79] demonstrating that our process does not leave residues on the TMD surfaces, unlike ref 80. We also avoid any extra contact between the PDMS stamp and the PICs. The PDMS stamp is aligned using x, y, z and theta (i.e., relative angle between PDMS stamp and target substrate) motorized stages to the microring area, and only contacts the target area of the PIC surface. This minimizes the area of contact, avoiding additional contamination with undesired $MoTe_2$ flakes from the PDMS stamp on top of the waveguide, which would induce extra losses.

Since our characterization technique can measure all the resonance frequencies covering the O- to E-band, the dispersion properties of the integrated hybrid microresonator can be calculated as well. These are critical for target applications at required wavelengths. E.g., anomalous dispersion is necessary for Kerr nonlinear photonics.[50] The measured integrated microresonator dispersion, defined as[72,81] $D_{int}(\mu) = \omega_\mu - \omega_0 - \mu D_1 = D_2\mu^2/2 + D_3\mu^3/6 + D_4\mu^4/24 + . . .$, is shown in Figure 3b, top. Here $\omega_\mu/2\pi$ is the frequency of the $\mu^{th}$ resonance, $D_1/2\pi$ is the microresonator FSR, $D_2/2\pi$ is the group-velocity dispersion, $D_3/2\pi$ and $D_4/2\pi$ are higher-order dispersion terms. The reference resonance frequency is $\omega_0/2\pi$ = 193.4 THz (corresponding to $\lambda_0$ = 1550 nm). Limited by the size of the transferred flake, the $D_{int}$ curves before and after transfer are nearly identical. To further investigate the dispersion change, the deviation from the $D_2$-dominant parabolic profile, defined as $[D_{int}(\mu) - D_2\mu^2/2]/2\pi$, is shown in Figure 3b, bottom. Higher-order dispersion changes (e.g., $D_3/2\pi$ and $D_4/2\pi$) and avoided mode crossings[81] are revealed. The measured parameters from fitting are $D_2/2\pi$ = 3.67 MHz and $D_3/2\pi$ = −3.2 kHz before 1L-MoTe$_2$ transfer, and $D_2/2\pi$ = 3.71 MHz and $D_3/2\pi$ = −4.2 kHz after transfer.

To confirm the coupling of the Si$_3$N$_4$ optical mode to 1L-MoTe$_2$, the same device is further characterized in the wavelength range 1050 - 1090 nm (near the 1L-MoTe$_2$ excitonic resonance ~1130 nm), using another ECDL operating in this wavelength range. A different microresonator with a gap distance ~370 nm between the bus waveguide and the microresonator is used, in which the small gap distance ensures sufficient evanescent coupling between bus waveguide and microresonator. Before 1L-MoTe$_2$ transfer, the mean loaded resonance line width is $\kappa/2\pi \sim$ 200 MHz. After transfer, most of the resonances, previously visible, vanish. The remaining resonances detected have $\kappa/2\pi >$ 1 GHz, corresponding to an *average* loss ~1.5 dB/cm near 1 $\mu$m wavelength. This value is averaged over the entire microresonator, despite the fact that only a small part of it is covered by 1L-MoTe$_2$. Comparing with the optical losses measured in the 1280−1630 nm range, this wavelength-dependent loss is consistent with the significant optical absorption ~3.4% at the 1L-MoTe$_2$ band edge[23] and confirms that 1L-MoTe$_2$ is coupled to the optical mode.

We then characterize the 1-THz-FSR microresonator with a ring radius of 22 $\mu$m. The smaller size leads to a large ratio of its perimeter covered by 1L-MoTe$_2$, $\eta\sim$ 13%. Figure 4a plots $\kappa/2\pi$ of the measured TE$_{00}$ resonances from 1355 to 1505 nm, before and after 1L-MoTe$_2$ transfer. The observed wavelength-dependence is due to the bus-waveguide-to-microresonator evanescent coupling (i.e., $\kappa_{ex}/2\pi$ is wavelength-dependent and is larger at longer wavelengths). For each resonance, due to 1L-MoTe$_2$ transfer, a line width increment $\Delta\kappa/2\pi$ of up to 80 MHz is observed. As 1L-MoTe$_2$ is thinner than 1 nm, and should not effect the evanescent coupling, we attribute this $\kappa/2\pi$ increment to the $\kappa_0/2\pi$ increment. Figure 4a inset shows a resonance at 1425 nm, after 1L-MoTe$_2$ transfer, where the Lorentzian fit gives $\kappa_{ex}/2\pi$ = 82 MHz and $\kappa_0/2\pi$ = 147 MHz, respectively. This indicates that 1L-MoTe$_2$ transfer introduces an extra loss. We estimate $Q_0 \approx 1.3 \times 10^6$, lower than the initial $Q_0 \approx 3.8 \times 10^6$. The *average* loss increment is ~0.15 dB/cm. Therefore, the estimated linear optical loss in the waveguide fully covered by 1L-MoTe$_2$ is $\alpha \approx 0.15 \times (13\%)^{-1}$ dB/cm = 1.2 dB/cm.

We also investigate the frequency shift of the resonance grid induced by 1L-MoTe$_2$. This provides information on the change of $n_{eff}$. Another identical microresonator is used as reference, on the same chip, 2.1 mm apart from that with 1L-MoTe$_2$. The absolute frequency of each TE$_{00}$ resonance is measured, before and after 1L-MoTe$_2$ transfer, for both microresonators. The relative frequency shift of each resonance, before and after transfer, is plotted in Figure 4b. The microresonator without 1L-MoTe$_2$ only has a small frequency shift ~1.8 GHz, likely due to environmental temperature change during measurement. The thermo-optic coefficient of Si$_3$N$_4$[82] is $dn(Si_3N_4)/dT$ = 2.5 × 10$^{-5}$/K. Thus, the temperature-induced frequency shift coefficient is −2.4 GHz/K (negative sign indicates red shift). For the microresonator with 1L-MoTe$_2$, an average frequency shift of −40.4 GHz is observed. Including the 1.8 GHz frequency shift identified in the reference microresonator, the total frequency shift due to 1L-MoTe$_2$ is −42.2 GHz. Since a part of the light field is coupled into 1L-MoTe$_2$, this frequency shift is induced by the increment of $n_{eff}$.

Finite-element-method (FEM) simulations of the TE$_{00}$ mode using COMSOL Multiphysics are then performed to study $n_{eff}$ and the resulting $\Delta n_{eff}$ due to the presence of 1L-MoTe$_2$. Figure 4c plots the simulated $n_{eff}$ and $\Delta n_{eff}$ as a function of Si$_3$N$_4$ waveguide height at 1550 nm. Here the waveguide has a fixed width $w$ = 1.45 $\mu$m and a varying height $h$ from 340 to 840 nm. We include in the simulations the 40 nm height difference between Si$_3$N$_4$ waveguide core and SiO$_2$ cladding. Surface current density boundary conditions are used to model 1L-MoTe$_2$. We use $n(MoTe_2)$ = 4.43,[23] with 0.7 nm layer thickness, close to the experimental value from AFM measurements[5,23].

The experimentally measured, *average* refractive index change is $\Delta n_{eff, avg} = n_{eff} \cdot \Delta f/f_0$, where $f_0$ is the resonance frequency and $\Delta f$ is the frequency shift. Considering that the Si$_3$N$_4$ microresonator is not fully covered by 1L-MoTe$_2$, we can write $\Delta n_{eff} = \Delta n_{eff, avg}/\eta$, where $\eta$ = 13% is the ratio of the microresonator perimeter covered by 1L-MoTe$_2$. Figure 4b gives $\Delta n_{eff}$ = 2.73 × 10$^{-3}$. This corresponds to the Si$_3$N$_4$ waveguide with $h$ = 475 nm, with ~0.3% of the optical mode overlapping the 1L-MoTe$_2$. In comparison, the SEM-measured waveguide height from the sample cross-section is $h$ = 540 nm, corresponding to $\Delta n_{eff}$ = 2.23 × 10$^{-3}$ in Figure 4c. Therefore, the experimental $\Delta n_{eff}$ is close to the simulated one and further confirms the successful coupling between MoTe$_2$ and Si$_3$N$_4$.

In conclusion, we demonstrated the integration of 1L-MoTe$_2$ on Si$_3$N$_4$ photonic microresonators with $Q_0$ = 1.3 × 10$^6$ for a 1-THz-FSR microresonator, and $Q_0$ = 3.9 × 10$^6$ for a 150-GHz-FSR one, with an optical loss of 1.2 dB/cm in the waveguide fully covered by 1L-MoTe$_2$ in the telecommunication bands. Our Si$_3$N$_4$ photonic Damascene process is thus compatibile with LM dry transfer. Wet transfer[1,35] and CVD growth[83−85] could also be used to integrate 1L-TMDs with larger surface areas. Combining this with low-loss Si$_3$N$_4$ spiral waveguides of extended lengths up to a meter,[45] high-responsivity, traveling-wave photodetectors could be built.[86] In addition, 1L-TMDs and single-layer graphene have a third-order-nonlinear susceptibility $\chi_3 \sim 10^{-18}$ m$^2$/V$^2$ (refs [87,88]) and $\chi_3 \sim 10^{-15}$ m$^2$/V$^2$ (refs [89−91]), significantly higher than that[38] of Si$_3$N$_4 \sim 10^{-21}$ m$^2$/V$^2$. Therefore, LM-integrated, high-Q Si$_3$N$_4$ microresonators could be used to realize few-photon nonlinear optics, TMD-assisted four-wave mixing, and

cavity-enhanced frequency conversion.[92] By maintaining the intrinsic low losses, our work paves the way to adding novel active functionalities on the $Si_3N_4$ photonics platform.[93]

## ■ AUTHOR INFORMATION

### Corresponding Authors

**Andrea C. Ferrari** − *Cambridge Graphene Centre, University of Cambridge, Cambridge CB3 0FA, U.K.*; ⊙ orcid.org/0000-0003-0907-9993; Email: acf26@eng.cam.ac.uk

**Tobias J. Kippenberg** − *Institute of Physics, Swiss Federal Institute of Technology Lausanne (EPFL), CH-1015 Lausanne, Switzerland*; Email: tobias.kippenberg@epfl.ch

### Authors

**Jijun He** − *Institute of Physics, Swiss Federal Institute of Technology Lausanne (EPFL), CH-1015 Lausanne, Switzerland*

**Ioannis Paradisanos** − *Cambridge Graphene Centre, University of Cambridge, Cambridge CB3 0FA, U.K.*; ⊙ orcid.org/0000-0001-8310-710X

**Tianyi Liu** − *Institute of Physics, Swiss Federal Institute of Technology Lausanne (EPFL), CH-1015 Lausanne, Switzerland*

**Alisson R. Cadore** − *Cambridge Graphene Centre, University of Cambridge, Cambridge CB3 0FA, U.K.*

**Junqiu Liu** − *Institute of Physics, Swiss Federal Institute of Technology Lausanne (EPFL), CH-1015 Lausanne, Switzerland*; ⊙ orcid.org/0000-0003-2405-6028

**Mikhail Churaev** − *Institute of Physics, Swiss Federal Institute of Technology Lausanne (EPFL), CH-1015 Lausanne, Switzerland*

**Rui Ning Wang** − *Institute of Physics, Swiss Federal Institute of Technology Lausanne (EPFL), CH-1015 Lausanne, Switzerland*

**Arslan S. Raja** − *Institute of Physics, Swiss Federal Institute of Technology Lausanne (EPFL), CH-1015 Lausanne, Switzerland*

**Clément Javerzac-Galy** − *Institute of Physics, Swiss Federal Institute of Technology Lausanne (EPFL), CH-1015 Lausanne, Switzerland*; ⊙ orcid.org/0000-0002-6816-1391

**Philippe Roelli** − *Institute of Physics, Swiss Federal Institute of Technology Lausanne (EPFL), CH-1015 Lausanne, Switzerland*

**Domenico De Fazio** − *Cambridge Graphene Centre, University of Cambridge, Cambridge CB3 0FA, U.K.*

**Barbara L. T. Rosa** − *Cambridge Graphene Centre, University of Cambridge, Cambridge CB3 0FA, U.K.*

**Sefaattin Tongay** − *School for Engineering of Matter, Transport and Energy, Arizona State University, Tempe, Arizona 85287, United States*; ⊙ orcid.org/0000-0001-8294-984X

**Giancarlo Soavi** − *Cambridge Graphene Centre, University of Cambridge, Cambridge CB3 0FA, U.K.; Institute for Solid State Physics, Friedrich-Schiller University Jena, 07743 Jena, Germany*; ⊙ orcid.org/0000-0003-2434-2251

Complete contact information is available at:
https://pubs.acs.org/10.1021/acs.nanolett.0c04149

### Author Contributions

‖(J.H., I.P.) These authors contributed equally to this work.

### Notes

The authors declare no competing financial interest.

The code and data used to produce the plots within this paper are available at DOI: 10.5281/zenodo.4527176.

## ■ REFERENCES

(1) Ferrari, A. C.; et al. Science and technology roadmap for graphene, related two-dimensional crystals, and hybrid systems. *Nanoscale* **2015**, *7*, 4598−4810.

(2) Wang, Q. H.; Kalantar-Zadeh, K.; Kis, A.; Coleman, J. N.; Strano, M. S. Electronics and optoelectronics of two-dimensional transition metal dichalcogenides. *Nat. Nanotechnol.* **2012**, *7*, 699−712.

(3) Manzeli, S.; Ovchinnikov, D.; Pasquier, D.; Yazyev, O. V.; Kis, A. 2D transition metal dichalcogenides. *Nat. Rev. Mater.* **2017**, *2*, 17033.

(4) Hui, F.; Grustan-Gutierrez, E.; Long, S.; Liu, Q.; Ott, A. K.; Ferrari, A. C.; Lanza, M. Graphene and related materials for resistive random access memories. *Adv. Electron. Mater.* **2017**, *3*, 1600195.

(5) Xia, F.; Wang, H.; Xiao, D.; Dubey, M.; Ramasubramaniam, A. Two-dimensional material nanophotonics. *Nat. Photonics* **2014**, *8*, 899−907.

(6) Krasnok, A.; Lepeshov, S.; Alú, A. Nanophotonics with 2D transition metal dichalcogenides. *Opt. Express* **2018**, *26*, 15972−15994.

(7) Romagnoli, M.; Sorianello, V.; Midrio, M.; Koppens, F. H. L.; Huyghebaert, C.; Neumaier, D.; Galli, P.; Templ, W.; D'Errico, A.; Ferrari, A. C. Graphene-based integrated photonics for next-generation datacom and telecom. *Nat. Rev. Mater.* **2018**, *3*, 392−414.

(8) Bonaccorso, F.; Sun, Z.; Hasan, T.; Ferrari, A. C. Graphene photonics and optoelectronics. *Nat. Photonics* **2010**, *4*, 611−622.

(9) Mueller, T.; Xia, F.; Avouris, P. Graphene photodetectors for high-speed optical communications. *Nat. Photonics* **2010**, *4*, 297−301.

(10) Sun, Z.; Martinez, A.; Wang, F. Optical modulators with 2D layered materials. *Nat. Photonics* **2016**, *10*, 227−238.

(11) Koppens, F. H. L.; Mueller, T.; Avouris, P.; Ferrari, A. C.; Vitiello, M. S.; Polini, M. Photodetectors based on graphene, other two-dimensional materials and hybrid systems. *Nat. Nanotechnol.* **2014**, *9*, 780−793.

(12) Mak, K. F.; Shan, J. Photonics and optoelectronics of 2D semiconductor transition metal dichalcogenides. *Nat. Photonics* **2016**, *10*, 216−226.

(13) Schaibley, J. R.; Yu, H.; Clark, G.; Rivera, P.; Ross, J. S.; Seyler, K. L.; Yao, W.; Xu, X. Valleytronics in 2D materials. *Nat. Rev. Mater.* **2016**, *1*, 16055.

(14) Zibouche, N.; Kuc, A.; Musfeldt, J.; Heine, T. Transition-metal dichalcogenides for spintronic applications. *Ann. Phys.* **2014**, *526*, 395−401.

(15) Radisavljevic, B.; Radenovic, A.; Brivio, J.; Giacometti, V.; Kis, A. Single-layer $MoS_2$ transistors. *Nat. Nanotechnol.* **2011**, *6*, 147−150.

(16) Withers, F.; Del Pozo-Zamudio, O.; Mishchenko, A.; Rooney, A. P.; Gholinia, A.; Watanabe, K.; Taniguchi, T.; Haigh, S. J.; Geim, A. K.; Tartakovskii, A. I.; Novoselov, K. S. Light-emitting diodes by band-structure engineering in van der Waals heterostructures. *Nat. Mater.* **2015**, *14*, 301−306.

(17) Novoselov, K. S.; Jiang, D.; Schedin, F.; Booth, T. J.; Khotkevich, V. V.; Morozov, S. V.; Geim, A. K. Two-dimensional atomic crystals. *Proc. Natl. Acad. Sci. U. S. A.* **2005**, *102*, 10451−10453.

(18) Mak, K. F.; Lee, C.; Hone, J.; Shan, J.; Heinz, T. F. Atomically Thin MoS$_2$: A New Direct-Gap Semiconductor. *Phys. Rev. Lett.* **2010**, *105*, 136805.

(19) Wang, G.; Chernikov, A.; Glazov, M. M.; Heinz, T. F.; Marie, X.; Amand, T.; Urbaszek, B. Colloquium: Excitons in atomically thin transition metal dichalcogenides. *Rev. Mod. Phys.* **2018**, *90*, 021001.

(20) Barbone, M.; Montblanch, A. R.-P.; Kara, D. M.; Palacios-Berraquero, C.; Cadore, A. R.; De Fazio, D.; Pingault, B.; Mostaani, E.; Li, H.; Chen, B.; Watanabe, K.; Taniguchi, T.; Tongay, S.; Wang, G.; Ferrari, A. C.; Atature, M.; et al. Charge-tuneable biexciton complexes in monolayer WSe$_2$. *Nat. Commun.* **2018**, *9*, 3721.

(21) Paradisanos, I.; Wang, G.; Alexeev, E. M.; Cadore, A. R.; Marie, X.; Ferrari, A. C.; Glazov, M. M.; Urbaszek, B. Efficient phonon cascades in hot photoluminescence of WSe$_2$ monolayers. *arXiv:2007.05369*, July 10, **2020**. arXiv.org e-Print archive. https://arxiv.org/abs/2007.05369 (accessed Feb 2, **2021**).

(22) Ross, J. S.; Wu, S.; Yu, H.; Ghimire, N. J.; Jones, A. M.; Aivazian, G.; Yan, J.; Mandrus, D. G.; Xiao, D.; Yao, W.; Xu, X. Electrical control of neutral and charged excitons in a monolayer semiconductor. *Nat. Commun.* **2013**, *4*, 1474.

(23) Ruppert, C.; Aslan, O. B.; Heinz, T. F. Optical Properties and Band Gap of Single- and Few-Layer MoTe$_2$ Crystals. *Nano Lett.* **2014**, *14*, 6231−6236.

(24) Robert, C.; Picard, R.; Lagarde, D.; Wang, G.; Echeverry, J. P.; Cadiz, F.; Renucci, P.; Högele, A.; Amand, T.; Marie, X.; Gerber, I. C.; Urbaszek, B. Excitonic properties of semiconducting monolayer and bilayer MoT$_2$. *Phys. Rev. B: Condens. Matter Mater. Phys.* **2016**, *94*, 155425.

(25) Engel, M.; Steiner, M.; Lombardo, A.; Ferrari, A. C.; Löhneysen, H. v.; Avouris, P.; Krupke, R. Light−matter interaction in a microcavity-controlled graphene transistor. *Nat. Commun.* **2012**, *3*, 906.

(26) Ross, J. S.; Klement, P.; Jones, A. M.; Ghimire, N. J.; Yan, J.; Mandrus, D. G.; Taniguchi, T.; Watanabe, K.; Kitamura, K.; Yao, W.; Cobden, D. H.; Xu, X. Electrically tunable excitonic light-emitting diodes based on monolayer WSe$_2$ p−n junctions. *Nat. Nanotechnol.* **2014**, *9*, 268−272.

(27) Bie, Y.-Q.; Grosso, G.; Heuck, M.; Furchi, M. M.; Cao, Y.; Zheng, J.; Bunandar, D.; Navarro-Moratalla, E.; Zhou, L.; Efetov, D. K.; Taniguchi, T.; Watanabe, K.; Kong, J.; Englund, D.; Jarillo-Herrero, P. A MoTe$_2$-based light-emitting diode and photodetector for silicon photonic integrated circuits. *Nat. Nanotechnol.* **2017**, *12*, 1124−1129.

(28) Javerzac-Galy, C.; Kumar, A.; Schilling, R. D.; Piro, N.; Khorasani, S.; Barbone, M.; Goykhman, I.; Khurgin, J. B.; Ferrari, A. C.; Kippenberg, T. J. Excitonic Emission of Monolayer Semiconductors Near-Field Coupled to High-Q Microresonators. *Nano Lett.* **2018**, *18*, 3138−3146.

(29) Datta, I.; Chae, S. H.; Bhatt, G. R.; Tadayon, M. A.; Li, B.; Yu, Y.; Park, C.; Park, J.; Cao, L.; Basov, D. N.; Hone, J.; Lipson, M. Low-loss composite photonic platform based on 2D semiconductor monolayers. *Nat. Photonics* **2020**, *14*, 256−262.

(30) Maiti, R.; Patil, C.; Saadi, M.; Xie, T.; Azadani, J.; Uluutku, B.; Amin, R.; Briggs, A.; Miscuglio, M.; Van Thourhout, D.; et al. Strain-engineered high-responsivity MoTe$_2$ photodetector for silicon photonic integrated circuits. *Nat. Photonics* **2020**, *14*, 578−584.

(31) Vahala, K. J. Optical microcavities. *Nature* **2003**, *424*, 839.

(32) Braginsky, V.; Gorodetsky, M.; Ilchenko, V. Quality-factor and nonlinear properties of optical whispering-gallery modes. *Phys. Lett. A* **1989**, *137*, 393−397.

(33) Cai, M.; Painter, O.; Vahala, K. J. Observation of critical coupling in a fiber taper to a silica-microsphere whispering-gallery mode system. *Phys. Rev. Lett.* **2000**, *85*, 74−77.

(34) Dhakal, K. P.; Roy, S.; Jang, H.; Chen, X.; Yun, W. S.; Kim, H.; Lee, J.; Kim, J.; Ahn, J.-H. Local Strain Induced Band Gap Modulation and Photoluminescence Enhancement of Multilayer Transition Metal Dichalcogenides. *Chem. Mater.* **2017**, *29*, 5124−5133.

(35) Bonaccorso, F.; Lombardo, A.; Hasan, T.; Sun, Z.; Colombo, L.; Ferrari, A. C. Production and processing of graphene and 2D crystals. *Mater. Today* **2012**, *15*, 564−589.

(36) Giambra, M. A.; Mi v s eikis, V.; Pezzini, S.; Marconi, S.; Montanaro, A.; Fabbri, F.; Sorianello, V.; Ferrari, A. C.; Coletti, C.; Romagnoli, M. Wafer-scale integration of graphene-based photonic devices. *arXiv: 2012.05816*, Nov. 18, 2020. arXiv.org e-Print archive. https://arxiv.org/abs/2012.05816 (accessed Feb 2, 2021).

(37) Soref, R. The Past, Present, and Future of Silicon Photonics. *IEEE J. Sel. Top. Quantum Electron.* **2006**, *12*, 1678−1687.

(38) Moss, D. J.; Morandotti, R.; Gaeta, A. L.; Lipson, M. New CMOS-compatible platforms based on silicon nitride and Hydex for nonlinear optics. *Nat. Photonics* **2013**, *7*, 597.

(39) Blumenthal, D. J. Photonic integration for UV to IR applications. *APL Photonics* **2020**, *5*, 020903.

(40) Krückel, C. J.; Fülöp, A.; Ye, Z.; Andrekson, P. A.; et al. Optical bandgap engineering in nonlinear silicon nitride waveguides. *Opt. Express* **2017**, *25*, 15370−15380.

(41) Xuan, Y.; et al. High-Q silicon nitride microresonators exhibiting low-power frequency comb initiation. *Optica* **2016**, *3*, 1171−1180.

(42) Ji, X.; Barbosa, F. A. S.; Roberts, S. P.; Dutt, A.; Cardenas, J.; Okawachi, Y.; Bryant, A.; Gaeta, A. L.; Lipson, M. Ultra-low-loss on-chip resonators with sub-milliwatt parametric oscillation threshold. *Optica* **2017**, *4*, 619−624.

(43) Ye, Z.; Twayana, K.; Andrekson, P. A.; Torres-Company, V. High-Q Si$_3$N$_4$ microresonators based on a subtractive processing for Kerr nonlinear optics. *Opt. Express* **2019**, *27*, 35719−35727.

(44) Liu, J.; Lucas, E.; Raja, A. S.; He, J.; Riemensberger, J.; Wang, R. N.; Karpov, M.; Guo, H.; Bouchand, R.; Kippenberg, T. J. Photonic microwave generation in the X- and K-band using integrated soliton microcombs. *Nat. Photonics* **2020**.14486

(45) Liu, J.; Huang, G.; Wang, R. N.; He, J.; Raja, A. S.; Liu, T.; Engelsen, N. J.; Kippenberg, T. J. High-yield wafer-scale fabrication of ultralow-loss, dispersion-engineered silicon nitride photonic circuits. *arXiv:2005.13949*, May 25, **2020**. arXiv.org e-Print archive. https://arxiv.org/abs/2005.13949 (accessed Feb 2, 2021).

(46) Selvaraja, S. K.; Heyn, P. D.; Winroth, G.; Ong, P.; Lepage, G.; Cailler, C.; Rigny, A.; Bourdelle, K. K.; Bogaerts, W.; Thourhout, D. V.; Campenhout, J. V.; Absil, P. Highly uniform and low-loss passive silicon photonics devices using a 300mm CMOS platform. *Optical Fiber Communication Conference*; OSA Publishing, Mar. 9−13, 2014; p Th2A.33.

(47) Ciminelli, C.; Dell'Olio, F.; Armenise, M. N.; Soares, F. M.; Passenberg, W. High performance InP ring resonator for new generation monolithically integrated optical gyroscopes. *Opt. Express* **2013**, *21*, 556−564.

(48) Gyger, F.; Liu, J.; Yang, F.; He, J.; Raja, A. S.; Wang, R. N.; Bhave, S. A.; Kippenberg, T. J.; Thévenaz, L. Observation of Stimulated Brillouin Scattering in Silicon Nitride Integrated Waveguides. *Phys. Rev. Lett.* **2020**, *124*, 013902.

(49) Foster, M. A.; Turner, A. C.; Sharping, J. E.; Schmidt, B. S.; Lipson, M.; Gaeta, A. L. Broad-band optical parametric gain on a silicon photonic chip. *Nature* **2006**, *441*, 960.

(50) Kippenberg, T. J.; Gaeta, A. L.; Lipson, M.; Gorodetsky, M. L. Dissipative Kerr solitons in optical microresonators. *Science* **2018**, *361*, eaan8083.

(51) Gaeta, A. L.; Lipson, M.; Kippenberg, T. J. Photonic-chip-based frequency combs. *Nat. Photonics* **2019**, *13*, 158−169.

(52) Wei, G.; Stanev, T. K.; Czaplewski, D. A.; Jung, I. W.; Stern, N. P. Silicon-nitride photonic circuits interfaced with monolayer MoS$_2$. *Appl. Phys. Lett.* **2015**, *107*, 091112.

(53) Rosser, D.; Fryett, T.; Ryou, A.; Saxena, A.; Majumdar, A. Exciton−phonon interactions in nanocavity-integrated monolayer transition metal dichalcogenides. *npj 2D Mater. Appl.* **2020**, *4*, 20.

(54) Gonzalez Marin, J. F.; Unuchek, D.; Watanabe, K.; Taniguchi, T.; Kis, A. MoS$_2$ photodetectors integrated with photonic circuits. *npj 2D Mater. Appl.* **2019**, *3*, 14.

(55) Gao, Y.; Zhou, G.; Tsang, H. K.; Shu, C. High-speed van der Waals heterostructure tunneling photodiodes integrated on silicon nitride waveguides. *Optica* **2019**, *6*, 514−517.

(56) Wilson, D. J.; Schneider, K.; Hönl, S.; Anderson, M.; Baumgartner, Y.; Czornomaz, L.; Kippenberg, T. J.; Seidler, P. Integrated gallium phosphide nonlinear photonics. *Nat. Photonics* **2020**, *14*, 57−62.

(57) Pfeiffer, M. H. P.; Herkommer, C.; Liu, J.; Morais, T.; Zervas, M.; Geiselmann, M.; Kippenberg, T. J. Photonic Damascene Process for Low-Loss, High-Confinement Silicon Nitride Waveguides. *IEEE J. Sel. Top. Quantum Electron.* **2018**, *24*, 1−11.

(58) Pfeiffer, M. H. P.; Liu, J.; Raja, A. S.; Morais, T.; Ghadiani, B.; Kippenberg, T. J. Ultra-smooth silicon nitride waveguides based on the Damascene reflow process: fabrication and loss origins. *Optica* **2018**, *5*, 884−892.

(59) Yang, Y.; Wu, J.; Xu, X.; Liang, Y.; Chu, S. T.; Little, B. E.; Morandotti, R.; Jia, B.; Moss, D. J. Invited Article: Enhanced four-wave mixing in waveguides integrated with graphene oxide. *APL Photonics* **2018**, *3*, 120803.

(60) Wu, J.; Yang, Y.; Qu, Y.; Jia, L.; Zhang, Y.; Xu, X.; Chu, S. T.; Little, B. E.; Morandotti, R.; Jia, B.; Moss, D. J. 2D Layered Graphene Oxide Films Integrated with Micro-Ring Resonators for Enhanced Nonlinear Optics. *Small* **2020**, *16*, 1906563.

(61) Zhang, X.; Lou, F.; Li, C.; Zhang, X.; Jia, N.; Yu, T.; He, J.; Zhang, B.; Xia, H.; Wang, S.; Tao, X. Flux method growth of bulk $MoS_2$ single crystals and their application as a saturable absorber. *CrystEngComm* **2015**, *17*, 4026−4032.

(62) Casiraghi, C.; Hartschuh, A.; Lidorikis, E.; Qian, H.; Harutyunyan, H.; Gokus, T.; Novoselov, K. S.; Ferrari, A. C. Rayleigh Imaging of Graphene and Graphene Layers. *Nano Lett.* **2007**, *7*, 2711−2717.

(63) Orchin, G. J.; De Fazio, D.; Di Bernardo, A.; Hamer, M.; Yoon, D.; Cadore, A. R.; Goykhman, I.; Watanabe, K.; Taniguchi, T.; Robinson, J. W. A.; Gorbachev, R. V.; Ferrari, A. C.; Hadfield, R. H. Niobium diselenide superconducting photodetectors. *Appl. Phys. Lett.* **2019**, *114*, 251103.

(64) Bromley, R. A.; Murray, R. B.; Yoffe, A. D. The band structures of some transition metal dichalcogenides. III. Group VIA: trigonal prism materials. *J. Phys. C: Solid State Phys.* **1972**, *5*, 759−778.

(65) Song, Q. J.; Tan, Q. H.; Zhang, X.; Wu, J. B.; Sheng, B. W.; Wan, Y.; Wang, X. Q.; Dai, L.; Tan, P. H. Physical origin of Davydov splitting and resonant Raman spectroscopy of Davydov components in multilayer $MoTe_2$. *Phys. Rev. B: Condens. Matter Mater. Phys.* **2016**, *93*, 115409.

(66) Trovatello, C.; et al. Strongly Coupled Coherent Phonons in Single-Layer $MoS_2$. *ACS Nano* **2020**, *14*, 5700−5710.

(67) Tan, P. H.; Han, W. P.; Zhao, W. J.; Wu, Z. H.; Chang, K.; Wang, H.; Wang, Y. F.; Bonini, N.; Marzari, N.; Pugno, N.; Savini, G.; Lombardo, A.; Ferrari, A. C. The shear mode of multilayer graphene. *Nat. Mater.* **2012**, *11*, 294−300.

(68) Zhang, X.; Han, W. P.; Wu, J. B.; Milana, S.; Lu, Y.; Li, Q. Q.; Ferrari, A. C.; Tan, P. H. Raman spectroscopy of shear and layer breathing modes in multilayer $MoS_2$. *Phys. Rev. B: Condens. Matter Mater. Phys.* **2013**, *87*, 115413.

(69) Pizzi, G.; Milana, S.; Ferrari, A. C.; Marzari, N.; Gibertini, M. Shear and breathing modes of layered materials. *arXiv:2011.14681*, Nov. 30, **2020**. arXiv.org e-Print archive. https://arxiv.org/abs/2011.14681 (accessed Feb 2, 2021).

(70) Goldstein, T.; Chen, S.-Y.; Tong, J.; Xiao, D.; Ramasubramaniam, A.; Yan, J. Raman scattering and anomalous Stokes−anti-Stokes ratio in $MoTe_2$ atomic layers. *Sci. Rep.* **2016**, *6*, 28024.

(71) Liu, J.; Raja, A. S.; Pfeiffer, M. H. P.; Herkommer, C.; Guo, H.; Zervas, M.; Geiselmann, M.; Kippenberg, T. J. Double inverse nanotapers for efficient light coupling to integrated photonic devices. *Opt. Lett.* **2018**, *43*, 3200−3203.

(72) Del'Haye, P.; Arcizet, O.; Gorodetsky, M. L.; Holzwarth, R.; Kippenberg, T. J. Frequency comb assisted diode laser spectroscopy

for measurement of microcavity dispersion. *Nat. Photonics* **2009**, *3*, 529−533.

(73) Liu, J.; Brasch, V.; Pfeiffer, M. H. P.; Kordts, A.; Kamel, A. N.; Guo, H.; Geiselmann, M.; Kippenberg, T. J. Frequency-comb-assisted broadband precision spectroscopy with cascaded diode lasers. *Opt. Lett.* **2016**, *41*, 3134−3137.

(74) Liu, J.; Raja, A. S.; Karpov, M.; Ghadiani, B.; Pfeiffer, M. H. P.; Du, B.; Engelsen, N. J.; Guo, H.; Zervas, M.; Kippenberg, T. J. Ultralow-power chip-based soliton microcombs for photonic integration. *Optica* **2018**, *5*, 1347−1353.

(75) Rosser, D.; Fryett, T.; Saxena, A.; Ryou, A.; Majumdar, A. High-precision local transfer of van der Waals materials on nanophotonic structures. *Opt. Mater. Express* **2020**, *10*, 645−652.

(76) Hemnani, R. A.; Tischler, J. P.; Carfano, C.; Maiti, R.; Tahersima, M. H.; Bartels, L.; Agarwal, R.; Sorger, V. J. 2D material printer: a deterministic cross contamination-free transfer method for atomically layered materials. *2D Mater.* **2019**, *6*, 015006.

(77) Purdie, D.; Pugno, N.; Taniguchi, T.; Watanabe, K.; Ferrari, A.; Lombardo, A. Cleaning interfaces in layered materials heterostructures. *Nat. Commun.* **2018**, *9*, 1−12.

(78) De Fazio, D.; Purdie, D. G.; Ott, A. K.; Braeuninger-Weimer, P.; Khodkov, T.; Goossens, S.; Taniguchi, T.; Watanabe, K.; Livreri, P.; Koppens, F. H.; et al. High-mobility, wet-transferred graphene grown by chemical vapor deposition. *ACS Nano* **2019**, *13*, 8926−8935.

(79) Montblanch, A. R.-P.; Kara, D. M.; Paradisanos, I.; Purser, C. M.; Feuer, M. S.; Alexeev, E. M.; Stefan, L.; Qin, Y.; Blei, M.; Wang, G., et al. Confinement of long-lived interlayer excitons in $WS_2/WSe_2$ heterostructures. *arXiv:2005.02416*, May 5, **2020** . arXiv.org e-Print archive. https://arxiv.org/abs/2005.02416 (accessed Feb 2, 2021).

(80) Jain, A.; Bharadwaj, P.; Heeg, S.; Parzefall, M.; Taniguchi, T.; Watanabe, K.; Novotny, L. Minimizing residues and strain in 2D materials transferred from PDMS. *Nanotechnology* **2018**, *29*, 265203.

(81) Herr, T.; Brasch, V.; Jost, J. D.; Mirgorodskiy, I.; Lihachev, G.; Gorodetsky, M. L.; Kippenberg, T. J. Mode spectrum and temporal soliton formation in optical microresonators. *Phys. Rev. Lett.* **2014**, *113*, 123901.

(82) Arbabi, A.; Goddard, L. L. Measurements of the refractive indices and thermo-optic coefficients of $Si_3N_4$ and $SiO_x$ using microring resonances. *Opt. Lett.* **2013**, *38*, 3878−3881.

(83) Lee, Y.-H.; Zhang, X.-Q.; Zhang, W.; Chang, M.-T.; Lin, C.-T.; Chang, K.-D.; Yu, Y.-C.; Wang, J. T.-W.; Chang, C.-S.; Li, L.-J.; Lin, T.-W. Synthesis of Large-Area $MoS_2$ Atomic Layers with Chemical Vapor Deposition. *Adv. Mater.* **2012**, *24*, 2320−2325.

(84) Kim, S.-Y.; Kwak, J.; Ciobanu, C. V.; Kwon, S.-Y. Recent Developments in Controlled Vapor-Phase Growth of 2D Group 6 Transition Metal Dichalcogenides. *Adv. Mater.* **2019**, *31*, 1804939.

(85) Wang, J.; Cheng, Z.; Chen, Z.; Xu, J.-B.; Tsang, H. K.; Shu, C. Graphene photodetector integrated on silicon nitride waveguide. *J. Appl. Phys.* **2015**, *117*, 144504.

(86) Wang, X.; Cheng, Z.; Xu, K.; Tsang, H. K.; Xu, J.-B. High-responsivity graphene/silicon-heterostructure waveguide photodetectors. *Nat. Photonics* **2013**, *7*, 888−891.

(87) Dai, Y.; Wang, Y.; Das, S.; Xue, H.; Bai, X.; Hulkko, E.; Zhang, G.; Yang, X.; Dai, Q.; Sun, Z. Electrical Control of Interband Resonant Nonlinear Optics in Monolayer $MoS_2$. *ACS Nano* **2020**, *14*, 8442−8448.

(88) Säynätjoki, A.; Karvonen, L.; Rostami, H.; Autere, A.; Mehravar, S.; Lombardo, A.; Norwood, R. A.; Hasan, T.; Peyghambarian, N.; Lipsanen, H.; Kieu, K.; Ferrari, A. C.; Polini, M.; Sun, Z. Ultra-strong nonlinear optical processes and trigonal warping in $MoS_2$ layers. *Nat. Commun.* **2017**, *8*, 893.

(89) Soavi, G.; et al. Broadband, electrically tunable third-harmonic generation in graphene. *Nat. Nanotechnol.* **2018**, *13*, 583−588.

(90) Soavi, G.; Wang, G.; Rostami, H.; Tomadin, A.; Balci, O.; Paradisanos, I.; Pogna, E. A. A.; Cerullo, G.; Lidorikis, E.; Polini, M.; Ferrari, A. C. Hot Electrons Modulation of Third-Harmonic Generation in Graphene. *ACS Photonics* **2019**, *6*, 2841−2849.

(91) Lafetá, L.; Cadore, A. R.; Mendes-de Sa, T. G.; Watanabe, K.; Taniguchi, T.; Campos, L. C.; Jorio, A.; Malard, L. M. Anomalous Nonlinear Optical Response of Graphene Near Phonon Resonances. *Nano Lett.* **2017**, *17*, 3447−3451.

(92) Majumdar, A.; Dodson, C. M.; Fryett, T. K.; Zhan, A.; Buckley, S.; Gerace, D. Hybrid 2D Material Nanophotonics: A Scalable Platform for Low-Power Nonlinear and Quantum Optics. *ACS Photonics* **2015**, *2*, 1160−1166.

(93) Youngblood, N.; Li, M. Integration of 2D materials on a silicon photonics platform for optoelectronics applications. *Nanophotonics* **2016**, *6*, 1205−1218.